LBL-32399
UC-404
Preprint

Lawrence Berkeley Laboratory
UNIVERSITY OF CALIFORNIA

Materials Sciences Division
National Center for Electron Microscopy

Submitted to Ultramicroscopy

"Resolution" in High-Resolution Electron Microscopy

M.A. O'Keefe

May 1992

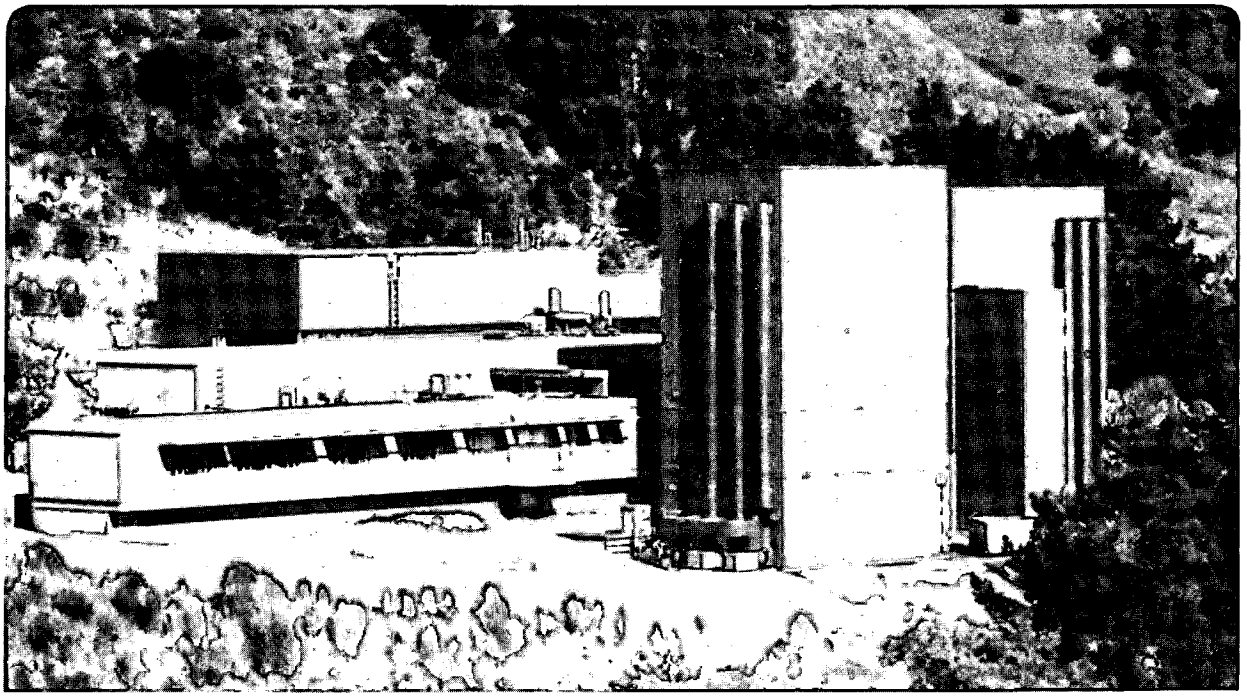

Prepared for the U.S. Department of Energy under Contract Number DE-AC03-76SF00098

DISCLAIMER

LBL-32399

"Resolution" in High-Resolution Electron Microscopy

M.A. O'Keefe

Materials Science Division
National Center for Electron Microscopy
Lawrence Berkeley Laboratory
University of California, Berkeley, CA 94720

Ultramicroscopy (submitted)

This work was supported in part by the Director, Office of Energy Research, Office of Basic Energy Sciences, Materials Science Division of the U.S. Department of Energy under Contract No. DE-AC03-76SF00098.

"RESOLUTION" IN HIGH-RESOLUTION ELECTRON MICROSCOPY

Michael A. O'KEEFE

National Center for Electron Microscopy, University of California, LBL, Berkeley, CA 94720

Submitted to Ultramicroscopy: 15 May 1992

Abstract

In the field of high-resolution transmission electron microscopy (HRTEM), the term "resolution" has come to hold a number of different meanings [1]. The present work reviews the various definitions of HRTEM resolution, derives theoretical expressions for resolution, and suggests how high resolutions may be attained in practice.

1. Introduction

In light optics, resolution can be defined for a particular microscope or optical system using the well-known Rayleigh criterion, which relates to the minimum distance where the separation of two points is barely discernable to the imaging wavelength and the aperture of the optical system. However, the Rayleigh resolution criterion was developed for incoherent imaging conditions and cannot, in general, be applied to high-resolution transmission electron microscopy (HRTEM). In fact, the Rayleigh criterion may lead to paradoxical results since it considers only two scatterers and does not account for the signal-to-noise ratio [2]. It may, however, be used for dark-field high-angle annular-detector (HAAD) STEM imaging [3,4]. For the case of strong multiple scattering in HRTEM lattice imaging, the only general relations that can be assumed between the image of a specimen and its projected crystal potential are those imposed by symmetry, and the "local" HRTEM column approximation. In fact, the effects of limited instrumental resolution may produce an image of lower symmetry than that of the object, whereas misalignment along symmetry axes may preserve some symmetry elements.

Under coherent conditions, the ability to distinguish atoms in an image depends on their scattering phases, which are a property of the sample. Since resolution, as defined classically by the Rayleigh criterion, should be a property of the microscope and not of the sample, it cannot be defined for HRTEM in the same terms. For HRTEM images in general (including images from thicker specimens, where dynamical contributions are strong), a way around this problem was found when computer programs [5] were developed to enable the comparison of experimental images with ones simulated from appropriate atomic models; such comparisons are usually made qualitatively, although the use of "R" factors based on least-square comparisons of computed and experimental images has been proposed [6,7]. Such R-factors should

emphasize the trade-off between resolution and noise. (At high count rates the noise from YAG scintillators is not Poisson; this distribution will affect the resolution retrieved by image processing from the new slow-scan YAG/CCD systems [1]).

2. Resolutions

Although we cannot, in general, produce a single figure that defines the resolution of an electron microscope, it is possible to talk about the resolution present in a particular electron micrograph, and even to place a limit on the resolution of images that can be produced by a particular HRTEM. Image "resolution" is a measure of the spatial frequencies transferred from the image amplitude spectrum (exit-surface wavefunction) into the image intensity spectrum (the Fourier transform of the image intensity). This transfer is affected by several factors -- the phases of the diffracted beams exiting the sample surface, additional phase changes imposed by the angular-dependent objective lens defocus and spherical aberration, the physical objective aperture, and coherence effects that can be characterized by the microscope spread-of-focus and incident beam convergence. For thicker crystals, the frequency-damping action of the coherence effects is complex and must be described in terms of the transmission cross-coefficient [8], but for a thin crystal, i.e. one behaving as a weak phase object (WPO), the damping action can best be described by quasi-coherent imaging theory [9] in terms of envelope functions [10,11] imposed on the usual phase-contrast transfer function (CTF).

There are three commonly employed definitions of "HRTEM resolution" [12]; since all are defined as the reciprocal of a particular spatial frequency, we need to examine how image amplitude terms are transferred into the image intensity spectrum. We can then examine how limits on these transfers arise from the effects of spatial and temporal coherence on the transmission cross-coefficient. The three resolutions are --

- "Fringe" resolution, or "line" resolution (sometimes called "lattice-plane" resolution), is measured from the highest spatial frequency present in the image intensity spectrum (and detectable in the optical diffractogram). In images from thicker crystals, it is generally over-optimistic compared with other measures of resolution, since it may come from a "second-order" or "non-linear" interference generating a half-spacing term with spatial frequency up to twice that of the highest-frequency diffracted beam passed by the objective aperture and the convergence cross-coefficient envelope [8]. For a properly aligned microscope, it is not affected by microscope spread-of-focus.
- "Linear-image" resolution, or "information limit" resolution, is measured by the highest spatial frequency transferred linearly from the amplitude spectrum to the intensity spectrum. Transferred frequencies fall within one or more passbands, but other (lower) frequencies may be blocked. Increased underfocus will push the convergence-limited damping function to

higher frequencies, thus the limit (called the information limit) to point resolution is a function of microscope spread-of-focus and mechanical stability.

• "Scherzer" resolution, or "structure-image" resolution (sometimes called "point" resolution or "point-to-point" resolution) is measured by the highest linearly-transferred spatial frequency that can be passed when no lower frequencies are blocked or passed with opposite phase [13]. The Scherzer image is important because it is (an approximation to) a projection of the specimen structure (to a limited resolution) in the direction of the incident beam. For images obtained at an "optimum" defocus of $\sqrt{1.5}$ Scherzers (that is, a defocus of $\sqrt{(1.5 C_S \lambda)}$, where C_S is the objective lens spherical aberration coefficient, and λ is the electron wavelength), the Scherzer resolution is generally defined by the upper limit of a passband with strong transfer out to a spatial frequency of $1.49 C_S^{-1/4} \lambda^{-3/4}$.

3. Resolution and the Image Intensity Spectrum

It is instructive to examine how the three resolutions relate to expressions that occur in the derivation of the weak-phase-object (WPO) image. The electron wavefield emerging from the exit surface of the specimen becomes the "object" for the imaging system of the electron microscope, which in turn produces the image intensity impinging on the recording medium. In general, the image intensity, $I(\mathbf{x})$, may be described as the square of the image amplitude, $\psi(\mathbf{x})$.

$$I(\mathbf{x}) = \psi(\mathbf{x}) \psi^*(\mathbf{x}) \tag{1}$$

The Fourier transform of the image intensity is called the image intensity spectrum, $I(\mathbf{k})$, and consists of a set of (complex) amplitudes in reciprocal space with the same spacings as the specimen diffraction pattern. Since the image intensity spectrum contains the same information as the image intensity itself, the whole process of image production in the HRTEM may be described in terms of general equations involving the image intensity spectrum, rather than by using the image intensity directly [14]. Such a description enables the various resolutions to be derived and contrasted. The equations also lead naturally to the notion of a transmission cross-coefficient [8] for incorporating spatial and temporal coherence effects (and are used in this manner in the SHRLI programs that have been so successful in generating HRTEM image simulations [15]). Fourier transformation of equation (1) yields the image intensity spectrum, $I(\mathbf{k})$, given by the auto-correlation function of the image amplitude spectrum, $\Psi(\mathbf{k})$, as

$$I(\mathbf{k}) = \Psi(\mathbf{k}) \otimes \Psi^*(-\mathbf{k}) \tag{2}$$

where $\otimes$ represents convolution, and $\Psi(\mathbf{k})$ is derived from the (Fourier space) specimen exit surface wavefield, $\Psi_E(\mathbf{k})$, by multiplication by the objective lens phase factor function, $\exp[i\chi(\mathbf{k})]$, where

$$\chi(\mathbf{k}) = \pi\varepsilon\lambda|\mathbf{k}|^2 + \pi C_S \lambda^3 |\mathbf{k}|^4/2 \qquad (3)$$

Here λ is electron wavelength, and ε and C_S are the objective lens defocus and spherical aberration coefficient respectively.

3.1 Fringe Images

Equation (2) states that any spatial frequency term in the general image intensity spectrum contains a combination of several of the spatial frequencies in the image amplitude spectrum (i.e. of many of the diffracted beams allowed through the objective aperture). Figure 1a illustrates how an intensity spectrum is generated from an amplitude spectrum for the case of an image formed from five co-linear diffracted beams out to h=±2. Note that the interferences making up the intensity spectrum terms may be classified as two types -- "linear" terms that involve the zero beam, and "non-linear" terms that occur when neither interfering beam is the zero beam. Although only five diffracted beams contribute to the image, there are nine peaks in the image intensity spectrum (and nine spots would appear in the optical diffractogram) representing terms out to h=±4. In this case the fringe resolution is the reciprocal of the 4 (or $\overline{4}$) frequency (formed by the "non-linear" interference of the 2 and $\overline{2}$ terms from the amplitude spectrum), that is, the fringe resolution is the reciprocal of the highest frequency in the intensity spectrum.

3.2 Linear (Information Limit) Images

If the non-linear or second-order interferences contributing to $I(\mathbf{k})$ in equation (2) can be neglected (*i.e.* if their amplitudes are much smaller than those of the linear interferences), it is possible to show that only one pair of diffracted beams contributes to each spatial frequency in the image intensity spectrum [14]. Furthermore, if the proportion of dynamical scattering is low enough to be neglected compared with kinematical scattering, then the two diffracted beams can be related back to *one* single coefficient of the projected specimen potential. The above two conditions hold for objects that scatter electrons only weakly, such as thin amorphous specimens and very thin crystalline specimens. Such a specimen may be treated as a weak-phase-object (WPO). Under the first condition, each term in the "linear-image" intensity spectrum consists of only two interference terms (fig 1b), *i.e.* the **k**th component of the "linear-image" intensity spectrum involves interferences of only the **k** and -**k** diffracted beams with the zero beam

$$I_L(\mathbf{k}) = \Psi(\mathbf{k}).\Psi^*(\mathbf{0}) + \Psi(\mathbf{0}).\Psi^*(-\mathbf{k}) \qquad (4)$$

and, since $\Psi(\mathbf{0})$ has a weight that is very close to unity for a weakly-scattering specimen,

$$I_L(\mathbf{k}) = \Psi_E(\mathbf{k}).\exp[i\chi(\mathbf{k})] + \Psi_E^*(-\mathbf{k}).\exp[-i\chi(-\mathbf{k})] \qquad (5)$$

For specimens that scatter electrons only weakly, it is possible to meet the second WPO condition also, *i.e.* to neglect dynamical diffraction and make a kinematic scattering approximation [16,17]. Under such an approximation, the exit-surface wavefield in direct space may be written

$$\Psi_E(\mathbf{x}) = 1 - i\sigma\phi_p(\mathbf{x})H \tag{6}$$

where σ is the interaction coefficient at the appropriate accelerating voltage, $\phi_p(\mathbf{x})$ is the specimen potential projected in the direction of the incident electron beam, and H is the specimen thickness through which the projection is taken. Transforming to Fourier space

$$\Psi_E(\mathbf{k}) = \delta(\mathbf{k}) - i\sigma V(\mathbf{k})H \tag{7}$$

where $V(\mathbf{k})$ is the **k**th Fourier component of the projected potential $\phi_p(\mathbf{x})$.

Substituting into (5),

$$I_L(\mathbf{k}) = \delta(\mathbf{k}) - i\sigma V(\mathbf{k})H\exp[i\chi(\mathbf{k})] + i\sigma V^*(-\mathbf{k})H\exp[-i\chi(-\mathbf{k})] \tag{8}$$

Since $V^*(-\mathbf{k})$ is equal to $V(\mathbf{k})$ for kinematic scattering, and $\{\exp[i\chi(\mathbf{k})] - \exp[-i\chi(-\mathbf{k})]\}$ is equal to $2i\sin\chi(\mathbf{k})$, the image intensity spectrum for such a "linear", or "weak-phase object" image is then

$$I_L(\mathbf{k}) = \delta(\mathbf{k}) + 2\sigma V(\mathbf{k})H\sin\chi(\mathbf{k}) \tag{9}$$

and the magnitude of the **k**th term in the image intensity spectrum is just proportional to $V(\mathbf{k})$, the **k**th Fourier coefficient of the projected potential, and to $\sin\chi(\mathbf{k})$, the value of the phase-contrast transfer function at the corresponding value of $|\mathbf{k}|$.

The significance of the $\sin\chi(\mathbf{k})$ factor in the expression for the terms making up the linear-image intensity spectrum can be illustrated geometrically. Figure 2 shows how the contribution of the **k**th term in the spectrum is governed by the value of $\sin\chi(\mathbf{k})$ under WPO conditions. The contribution to the $\Psi(\mathbf{k})$ term of the image amplitude spectrum (eqn 4) is shown in figure 2a. In the complex (Argand) plane, the **k**th Fourier coefficient of the projected potential $V(\mathbf{k})$ can be represented by a complex number lying along some direction (in the figure, we have chosen the case of a centrosymmetric crystal, and $V(\mathbf{k})$ lies along the positive-real axis). Under the kinematic scattering approximation (eqn 7), diffraction produces the **k**th component of the exit-surface wave $\Psi_E(\mathbf{k})$ in the form of the diffracted beam scattering from $V(\mathbf{k})$; then $\Psi_E(\mathbf{k})$ can be represented by a complex number, rotated $-\pi/2$ from $V(\mathbf{k})$ and equal to $-i\sigma V(\mathbf{k})H$. To form the image, the diffracted beam propagates from the exit surface to the

image plane; at the image plane, the phase of $\Psi_E(\mathbf{k})$ has been changed by the action of the lens to form the kth component of the image amplitude spectrum $\Psi(\mathbf{k})$, represented by the complex number rotated by an angle of $\chi(\mathbf{k})$ from $\Psi_E(\mathbf{k})$.

Under the linear-image approximation, the image intensity spectrum is derived from the image amplitude spectrum by addition of just two terms (eqn 4); thus the kth component of the image intensity spectrum $I_L(\mathbf{k})$ is the sum of $\Psi(\mathbf{k})$ and $\Psi^*(-\mathbf{k})$. Just as figure 1a shows how $\Psi(\mathbf{k})$ can be represented geometrically, figure 1b illustrates the geometrical representation of $\Psi^*(-\mathbf{k})$. Then the kth component of the image intensity spectrum, the sum of $\Psi(\mathbf{k})$ and $\Psi^*(-\mathbf{k})$, is shown in figure 2c. From the figure, we see that $I_L(\mathbf{k})$ is just twice the projection of $\Psi(\mathbf{k})$ onto the negative extension of $V(\mathbf{k})$ (as in eqn 9), and the projection of $\Psi(\mathbf{k})$ is proportional to $V(\mathbf{k})$ times $\sin\chi(\mathbf{k})$. This proportionality demonstrates the importance of the $\sin\chi$ term. Obviously, $I_L(\mathbf{k})$ is maximized as the lens phase $\chi(\mathbf{k})$ approaches a value of $-\pi/2$, and falls to zero as $\chi(\mathbf{k})$ approaches zero (or $n\pi$). Thus $\sin\chi$ is a weighting term that governs how much of each term in the image amplitude spectrum is transferred into the image intensity spectrum. For this reason, $\sin\chi$ is called the *contrast* transfer function (CTF).

More properly perhaps, $\sin\chi$ should be called the *phase-contrast* transfer function, in order to stress that it describes the transfer of only the linear-image, or first-order, terms into the intensity, as described by the thin-crystal, or weak-phase-object approximation. Also, some authors use the term CTF to refer to $2\sin\chi$ because the value of $I_L(\mathbf{k})$ is twice the projection of $\Psi(\mathbf{k})$, *i.e.* $\Psi(\mathbf{k})$ times twice $\sin\chi(\mathbf{k})$, so that the transfer of $\Psi(\mathbf{k})$ into $I_L(\mathbf{k})$ is described by $2\sin\chi$.

A plot of $\sin\chi(\mathbf{k})$ as a function of $|\mathbf{k}|$ provides information as to how each diffracted beam will transfer into the image. Some CTF curves are shown in figure 3. For any particular objective lens polepiece and microscope accelerating voltage, the only adjustable parameter in the expression for $\chi(\mathbf{k})$ is the defocus (eqn 3). Changing defocus gives us some control over the shape of the CTF curve, and thus the amount of transfer into the image of the available diffracted beams.

3.3 Scherzer Images

Scherzer [13] introduced the concept of the transfer function and suggested an optimum defocus condition designed to maximize the range of spatial frequencies for which $\sin\chi$ is close to $-\pi/2$. Scherzer chose the value of optimum defocus to be $-2.5\sqrt{(C_S\lambda/2\pi)}$, or approximately $-\sqrt{(C_S\lambda)}$; this value of defocus is now called one Scherzer. Figure 3a shows a CTF curve for a defocus of one Scherzer. At this defocus, the objective lens phase angle χ has a value close to

zero for zero frequency (large spacings), reaches a value of $-\pi/2$ ($\sin\chi = -1$) for spatial frequencies around $C_S^{-1/4}\lambda^{-3/4}$, and returns to zero at a frequency of $\sqrt{2}C_S^{-1/4}\lambda^{-3/4}$; it then changes sign and becomes positive. As long as $\sin\chi(\mathbf{k})$ remains negative, then $I_L(\mathbf{k})$ will be opposite in sign to its originating $V(\mathbf{k})$. Thus, at a (real-space) position where a component $V(\mathbf{k})$ contributes to a positive peak in the crystal potential $\phi(\mathbf{x})$, the corresponding image intensity component $I_L(\mathbf{k})$ will show a minimum in the image intensity at this position; since positive peaks in the crystal potential occur at atom positions, we say that Scherzer defocus produces a "black-atom" condition.

Beyond the "Scherzer cut-off frequency" $\sin\chi(\mathbf{k})$ becomes positive, and higher-frequency Fourier components of the potential would contribute to the image with opposite sign ("white-atom" contrast) to those below the cut-off. An image containing a mixture of spatial frequencies transferred with opposite phases is, in general, no longer interpretable intuitively and requires comparison with image simulations for interpretation [5]. For this reason, frequencies above the Scherzer cut-off are frequently blocked, either with an objective aperture or by coherence effects, in order to provide a simple image. Since no frequency higher than the Scherzer cut-off frequency can be guaranteed to be transferred with the correct phase, such a "Scherzer" image will have a resolution no greater than the reciprocal of the cut-off frequency.

Although those image amplitude components with spatial frequencies lying within the broad Scherzer passband will be transferred into the image intensity spectrum with various weightings (as shown by figure 3a), usual practice is to make the approximation that transfer is complete for each frequency, *i.e.* that $\sin\chi(\mathbf{k})$ is equal to -1 from zero spatial frequency to the cut-off frequency. Then, with $\sin\chi = -1$ in equation 9, the Scherzer image intensity spectrum is given by

$$I_S(\mathbf{k}) = \delta(\mathbf{k}) - 2\,\sigma H\, V(\mathbf{k}) \qquad (10)$$

Fourier transformation of this expression yields the Scherzer image intensity as

$$I_S(\mathbf{x}) = 1 - 2\,\sigma H\, \phi_p(\mathbf{x}) \qquad (11)$$

where, (as for eqn 6), σ is the interaction coefficient at the appropriate accelerating voltage, $\phi_p(\mathbf{x})$ is the specimen potential (to a limited resolution) projected in the direction of the incident electron beam, and H is the specimen thickness through which the projection is taken. Equation 11 shows that the image intensity of the Scherzer image is proportional to the negative of the specimen potential projected in the beam direction, *i.e.* minima in the Scherzer image correspond to maxima in the specimen potential ("black atom" condition).

It is easy to compute "perfect Scherzer" or "WPO" images according to equation 11, and these images are useful for checking on the resolution of more-complicated images, even ones simulated for novel conditions such as hollow-cone dark-field imaging [18]. Comparisons of simulated WPO and experimental images show that using the cut-off value to determine the Scherzer resolution of HRTEMs may be optimistic, since resolution in experimental images may be up to 10% less than the Scherzer cut-off value [18], because higher frequencies are not transferred with their full weight (*e.g.* in figure 3a, a diffracted beam corresponding to a spacing of 1.9Å is passed with only 50% weighting, although the Scherzer cut-off is nominally 1.78Å).

Scherzer Resolution

It is possible to extend the passband for the Scherzer image by setting defocus to be slightly further underfocus than one Scherzer. Cowley [17] suggested a defocus value of $\sqrt{(4/3)}$ Scherzers, and a value of $\sqrt{(1.42)}$ was judged best for single-atom imaging [19]. Once simulated images became available, a defocus value of $\sqrt{(3/2)}$ Scherzers was decided upon, based on careful comparisons of simulated WPO and SHRLI images [15], and this is the value that is generally accepted as "optimum" [7]. At this optimum defocus value, $\chi(\mathbf{k})$ reaches a minimum of $-3\pi/4$ at a spatial frequency of $1.1067C_S^{-1/4}\lambda^{-3/4}$ (compared with a minimum value of $-\pi/2$ at $C_S^{-1/4}\lambda^{-3/4}$ for a defocus of one Scherzer). Because $\chi(\mathbf{k})$ dips below $-\pi/2$, the CTF curve shows a mid-range hump (fig.3b), reaching a maximum value of $-1/\sqrt{2}$, so that mid-range spatial frequencies within the passband are transferred with as little as 70% weighting. In fact, comparison with simulations shows that it makes sense to consider the passband as extending over the spatial frequency region within which transfer is always greater than 70%. In terms of the Argand diagrams of figure 2, this means that only amplitude components with phase angles within $\pm\pi/4$ of the negative extension of $V(\mathbf{k})$ are considered as contributing fully to the Scherzer image. This passband is marked on figure 3b and extends from $0.4741C_S^{-1/4}\lambda^{-3/4}$ to $1.4916C_S^{-1/4}\lambda^{-3/4}$ [14]. Choosing the Scherzer resolution of the microscope as the reciprocal of the latter figure defines it to be

$$d_S = 0.67\ C_S^{1/4}\,\lambda^{3/4} \qquad (12)$$

Since the Scherzer resolution for any HRTEM depends on both the electron wavelength and the spherical aberration coefficient, it may be improved by reducing either (or both). From equation 12, any decrease in wavelength will have three times the effect of a similar decrease in C_S. For this reason, the evolution of the HRTEM has led to a range of high-voltage microscopes like the 1Mev JEOL ARM-1000, and even the "standard" lower-voltage microscope voltage has been increased from 100keV to 200keV. In addition, a group of newer mid-voltage (300-400keV) HRTEMs are now achieving sub-2Å resolutions. A list of HRTEMs, showing accelerating voltages and C_S values, is given in table 1.

4. Resolution and Coherence Effects

The limit to Scherzer resolution is determined by the objective lens phase angle $\chi(\mathbf{k})$ at optimum defocus. This angle is, in turn, ultimately determined by C_S and λ (eqn 12). However there exist additional limits, imposed by coherence conditions, that also determine the weighting with which image amplitude components transfer into the image intensity spectrum.

In all HRTEM images, the incident electron beam suffers from the effects of limited spatial and temporal coherence. These effects produce a smearing of the image, and provide the ultimate limits on how high a spatial frequency can be transferred into the image. The effect of partial temporal coherence is manifested as a spread of focus, and that of partial spatial coherence as incident beam convergence producing an angular variation within each diffracted beam [20]. Coherence effects have different actions on the transfer of linear and non-linear terms into the image intensity spectrum, and thus produce different limits on linear and non-linear images.

4.1 Information Limit (Linear-Image) Resolution

Frank [10] showed that the resolution-limiting effects of partial coherence on linear (WPO) images could be described in reciprocal space as "damping envelope" functions that multiply the usual CTF curve. The envelope for spread of focus has the form

$$E_\Delta(\mathbf{k}) = \exp\{-\tfrac{1}{2}\pi^2\lambda^2\Delta^2\mathbf{k}^4\} \tag{13}$$

where Δ is the halfwidth of a Gaussian spread-of-focus that models the fact that the recorded image is the sum of many images all at slightly different values of focus. The envelope for incident beam convergence has the form

$$E_\alpha(\mathbf{k}) = \exp\{-\pi^2\alpha^2(\varepsilon+\lambda^2C_S\mathbf{k}^2)^2\mathbf{k}^2\} \tag{14}$$

where α is the semi-angle of the convergence cone at the specimen surface, and specifies the range of angles (of misorientation with respect to the optic axis) over which images are formed and added into the recorded image [20].

The effects of $E_\alpha(\mathbf{k})$ and $E_\Delta(\mathbf{k})$ on the CTF curve of figure 3b can be seen in figures 4a and 4b respectively. Here the α and Δ have been assigned typical values of 1milliradian and 60Å. Note how the transfer of higher-frequency amplitude components is heavily damped in both cases. Although it is difficult to assign "cutoff" frequencies because the envelope functions slope gradually to zero, especially in the case of the $E_\Delta(\mathbf{k})$ envelope where the slope is more gradual (fig 4b), we can choose to set the cutoff frequencies at the value of exp(-2) or 13.7%, and produce cutoffs from the expressions for $E_\alpha(\mathbf{k})$ and $E_\Delta(\mathbf{k})$ as [18]

$$|\mathbf{k}|_\Delta = (\pi\lambda\Delta/2)^{-1/2} \tag{15}$$

and

$$|\mathbf{k}|_\alpha = S_+^{1/3} + S_-^{1/3} \qquad \text{where} \qquad S_\pm = \left[\frac{3.3}{4\pi\alpha} \pm \sqrt{\frac{\varepsilon^3}{27C_S\lambda^2} + \left(\frac{3.3}{4\pi\alpha}\right)^2} \right] / C_S\lambda^2 \tag{16}$$

where (16) holds for values of defocus larger (more positive) than $-1.23C_S^{1/3}(\lambda/\alpha)^{2/3}$.

For the conditions of figure 4, the cutoff limit due to $E_\alpha(\mathbf{k})$ is 1.42Å (fig 4a) and that due to $E_\Delta(\mathbf{k})$ is 1.25Å (fig 4b)†. Note that, although $E_\alpha(\mathbf{k})$ has a lower cutoff because it falls to exp(-2) faster than $E_\Delta(\mathbf{k})$, it has less effect within the Scherzer passband because its slope is not as shallow as that of $E_\Delta(\mathbf{k})$. The combined effect of the two damping envelopes is to reduce transfer both within and without the Scherzer passband giving a combined cutoff near 1.5Å (fig.4c). Thus the information limit in a micrograph recorded under these conditions would be 1.5Å.

Interestingly, the actions of the $E_\alpha(\mathbf{k})$ and $E_\Delta(\mathbf{k})$ envelopes (their shapes) appear very similar for the mid-voltage microscope conditions of figure 4. Earlier matching of simulated and experimental images by O'Keefe [21] showed that the damping envelope that was limiting the resolution of a low-voltage (100keV) HRTEM was not the same as the one limiting a high-voltage (1MeV) HRTEM; at optimum defocus the low-voltage TEM was limited by convergence and the high-voltage TEM was limited by spread of focus (fig 5).

Information Limit Resolution

Although the combined effect of the $E_\alpha(\mathbf{k})$ and $E_\Delta(\mathbf{k})$ envelopes leads to a 1.5Å information limit for the image obtained under the conditions of fig 4c, this figure is not necessarily the information limit of the microscope (although we could call it the "Scherzer-image information limit"). Because the $E_\alpha(\mathbf{k})$ envelope changes shape with change in defocus (eqn 14), so does the convergence cutoff frequency $|\mathbf{k}|_\alpha$ (eqn 16). Figure 6a,b shows this effect for zero spread-of-focus. At a defocus value of 1.225 Scherzers (fig 6a), the $|\mathbf{k}|_\alpha$ value is 1.42Å, but at 2.345 Scherzers (fig 6b), it is 1.25Å. Although the image obtained under condition (b) is not a Scherzer image, it is still a linear image, and contains information out to 1.25Å. By increasing the amount of underfocus, we can continue to obtain ever higher-frequency information -- at 3.082 Scherzers defocus the value of $|\mathbf{k}|_\alpha$ is 1.16Å. Thus it is clear that the effect of convergence does not constitute an information limit for the microscope. However, the effect of spread-of-focus does do so. If spread-of-focus is included in the CTF

† The expressions (15) and (16) for $|\mathbf{k}|_\Delta$ and $|\mathbf{k}|_\alpha$ are programmed into the Fortran program HP as the functions LIMD and LIMA. This program is available as source code from the EMSA EMPPDL.

plots for larger underfocus, we find that all CTF plots for the microscope lie within the $E_\Delta(\mathbf{k})$ envelope (fig 6c), and no linear-image information can be transferred at any frequency higher than $E_\Delta(\mathbf{k})$. Thus, from eqn 15, the information limit resolution of the microscope is given by

$$d_L = 1/|\mathbf{k}|_\Delta = \sqrt{(\pi\lambda\Delta/2)} \tag{17}$$

And this expression shows that the information limit is dependent only on λ and Δ. Thus, for a microscope at a given accelerating voltage, any decrease in Δ will improve the information limit of that microscope. In order to reduce Δ we must reduce one or more of the factors contributing to the spread of focus. Since the focal length of a magnetic lens is proportional to V/I^2, where V is the accelerating voltage and I is the lens current, we can write an expression for Δ as [14]

$$\Delta = C_C \sqrt{[(\delta V/V)^2 + (2\delta I/I)^2 + (\delta E/E)^2]} \tag{18}$$

where C_C is the chromatic aberration coefficient for the objective lens, $\delta V/V$ is the fractional change in voltage over the time scale of image acquisition, $\delta I/I$ is the fractional change in lens current, and $\delta E/E$ is the energy spread in the electron beam as a fraction of the total energy. Also, any vertical vibration of the specimen with respect to the lens will contribute to Δ.

For the examples shown (figs 4&6), Δ was estimated by taking the fractional changes in voltage and current to be one part per million, and δE to be one electron volt. Then

$$\Delta = 1.65\text{x}10^7 \sqrt{[(10^{-6})^2 + (2\text{x}10^{-6})^2 + (1/400{,}000)^2]}\ \text{Å} \approx 60\text{Å} \tag{19}$$

To improve the information limit, Δ could be reduced by reducing any of C_C, δV, δI, or δE. The first three would involve the microscope manufacturer, but δE can be minimized by reducing beam intensity with the gun bias control. Of course the best way to reduce δE is to use a field-emission-gun electron source (FEG) with a δE value in the range of 0.3 to 0.7eV. For a value of 0.3eV, Δ for the above HRTEM would reduce to approximately 40Å, bringing the microscope information limit resolution close to 1Å. HRTEMs capable of accepting FEGs are marked in Table 1.

4.2 Fringe Resolution

The concept of the damping envelope can be extended to incorporate the effects of partial coherence on non-linear interferences by means of the transmission cross-coefficient. Fejes [22] derived the transmission cross-coefficient for the case of temporal coherence, and O'Keefe [8] formulated the equivalent function for spatial coherence; later, Ishizuka [23] produced a summary of their work. The transmission cross-coefficient assigns a damping factor to every pair-wise interference term (fig 1a) that is summed to form an image intensity component. Plots of typical damping functions (fig 7) reveal that neither α nor Δ blocks the transference of interferences, of the form $\Psi(\mathbf{n}).\Psi^*(\mathbf{n})$, that contribute to the zero-frequency image intensity

component (lying along the positive diagonal in fig 7). In addition, interferences of the form $\Psi(\mathbf{n}).\Psi^*(-\mathbf{n})$ (lying along the negative diagonal) are never blocked by Δ, and are blocked by α only for large $|\mathbf{n}|$. If the values of defocus and α are chosen so as to allow a particular linear-image $\Psi(\mathbf{n}).\Psi^*(0)$ interference to be undamped by α, then the corresponding non-linear interference $\Psi(\mathbf{n}).\Psi^*(-\mathbf{n})$ will be undamped by both α and Δ (even if the linear interference $\Psi(\mathbf{n}).\Psi^*(0)$ is blocked by Δ); in this case, the image will contain half-period spacings corresponding to an intensity spectrum component of frequency $2|\mathbf{n}|$. For large values of underfocus and thicker specimens, fringe resolution can greatly exceed the information limit. Under these conditions an image of SiC with an apparent resolution of 1.09Å can be produced by a HRTEM with an information limit of 1.8Å [24]. Although images containing a large proportion of second-order interferences require interpretation via comparisons with simulated images, the fact that they may contain information beyond the "information limit" makes them potentially useful.

Because interferences of the form $\Psi(\mathbf{n}).\Psi^*(-\mathbf{n})$ are never damped by Δ, and a suitable value of defocus can move the α-function passband to transfer arbitrarily-high frequencies, it would appear that the fringe resolution of the microscope has no limit. However, (horizontal) mechanical vibration of the specimen will blur out high frequencies (vertical vibration is included in Δ). Also, slight misalignments of the microscope will cause the positions of the non-linear interference terms to "slide off" the white bands of the α and Δ damping functions (fig 7); these bands become much narrower at higher frequencies.

Fringe Resolution

In any particular image, the non-linear α damping function will permit the formation of half-period fringes at half the spacing corresponding to the $|\mathbf{k}|_\alpha$ value given by equation (16) for the chosen value of defocus. Thus the fringe resolution in the image will be given by

$$d_F = 0.5/|\mathbf{k}|_\alpha \qquad (18)$$

The overall fringe resolution limit of the microscope will be determined by (horizontal) mechanical vibration of the specimen, and microscope alignment accuracy.

5. Operating Considerations

WPO Conditions

It is possible to establish experimentally, from micro-CBED patterns of the image area or from optical diffractograms, that a given HRTEM object is behaving as a WPO. Then the phase change due to scattering is exactly $-\pi/2$, and the bright-field HRTEM image can be considered as an axial electron hologram. The WPO approximation solves the "object reconstruction"

problem by relating the exit face wavefunction to the object (the "image reconstruction" problem involves the removal, by image processing, of unwanted electron-optical lens aberrations).

High-Voltage Microscopes

For low and mid-voltage HRTEMs, the information limit resolution (eqn 17) generally exceeds the Scherzer-image resolution (eqn 12). This is generally not true for high-voltage HRTEMs, in which high-voltage ripple can produce large values of Δ, and hence severe damping by the linear-image envelope function $E_\Delta(\mathbf{k})$. In fact, mid and high-voltage microscopes can have very similar information limit resolutions, although they might have very different Scherzer resolutions. A comparison (fig 8) of the CTF curves for a 400keV HRTEM (C_S=1mm) with a 1Mev HRTEM (C_S=2.3mm), shows that transfer down to 1.7Å is similar, but that the 400keV CTF (curve 1) reverses the sign of higher frequencies, whereas the 1MeV (curve 2) transfers without sign reversal. On the other hand, frequencies near the nominal Scherzer resolution of the 1MeV HRTEM (1.32Å) are not passed with significant weight. Figure 8 also shows a CTF for a 1.25MeV HRTEM (curve 3), predicting transfer to below 1.2Å if Δ can be reduced to 100Å. Note that it is easy to define the Scherzer resolution as 1.7Å for curve 1, but the shallow slopes of the CTFs of the high-voltage HRTEMs makes it difficult to produce a clear definition of linear-image resolution in a Scherzer image from these microscopes.

Resolution Extension

Scherzer resolutions can be improved by reducing values of C_S and by increasing microscope beam energy. The first course will continue to be followed by the manufacturers of mid-voltage HRTEMs, and the second by the high-voltage aficionados. However, there are problems with both of these approaches. The art of high-resolution microscopy generally requires a reasonable degree of tilt in the microscope stage, but the smaller stage dimensions associated with reduced C_S make large tilts difficult. At higher voltages, beam-induced specimen damage can limit the range of specimens that can be examined, and reduce the time available for observing others. Low-dose techniques and sensitive CCD detectors may help mitigate this problem.

For microscopes in which the information limit resolution is much better than the Scherzer resolution, amplitude components can be transferred at frequencies beyond the Scherzer resolution by going further underfocus (fig 6). Because the image now contains bands of frequencies with different phases, interpretation is no longer straightforward; however the extra information (*i.e.* extra to that present in the Scherzer image) can be used to interpret the structure via comparison with image simulations. Anstis and O'Keefe [25] noted that, although at Scherzer defocus the 100keV TEM of figure 5a could not resolve the small tunnels in the

$Nb_{12}O_{29}$ specimen, they could be seen in an image taken with increased underfocus (although the regions of the image showing the large tunnels were now scrambled). This result was confirmed with image simulation [25].

Instead of comparing through-focus series with image simulations to derive information about structural features smaller than the Scherzer resolution (but larger than the information limit), various image reconstruction schemes have been proposed. Some of these schemes combine the information present in a focal series of images into one image, in effect extending the Scherzer resolution to the information limit [26,27]. One procedure has reached 1Å resolution in perchlorocoronene by combining information from the image and the diffraction pattern [28]. Another procedure [29] resolved atoms by producing sections through a staurolite specimen at 1.6Å resolution (although atoms can be arbitrarily close in projection, they are never closer than 1.6Å in a section). For those schemes that involve division by the CTF, high-voltage microscopes may hold an advantage, since there are fewer (or no) zeros in the CTF all the way to the information limit (fig 8). By dividing a focal series of intensity spectra by the spread-of-focus envelope function for the ARM-1000 operating at 800keV, another procedure produced reconstructions with a resolution of 1.38Å under conditions where the useful "Scherzer information limit" resolution of the microscope was 1.6Å [30].

Conclusions

For a HRTEM, it is possible to define several resolutions, some reflecting the limits of the microscope, others pertaining to a particular micrograph produced with that microscope.

Scherzer Resolution: A working definition for the Scherzer resolution d_S of a microscope is supplied by eqn 12. Note that the Scherzer resolution of a particular micrograph may be lower than d_S depending upon the spatial frequencies of the beams diffracted from the specimen, since the Scherzer resolution of the micrograph will be limited to the highest frequency that is transferred.‡

Information Limit: The information limit d_L for a HRTEM is dependent solely on the spread of focus (eqn 17), which may be estimated from equation 18, and mechanical stability. The information limit for any particular micrograph may be worse than d_L because of the defocus-dependent effect of incident beam convergence (eqn 16).

Fringe Resolution: It is difficult to place a limit on the fringe resolution of a HRTEM, since it is ultimately determined by the mechanical stability of the microscope and the precision of its alignment. The fringe resolution of a particular micrograph is limited to twice the convergence

‡ The 400keV *microscope* of figure 8 has a Scherzer resolution close to 1.7Å. However its Scherzer *micrograph* of a perfect [110] silicon specimen will have a resolution of only 1.92Å because only the 111 and 220 diffracted beams will be transferred from the amplitude spectrum into the image intensity spectrum (at spatial frequencies corresponding to spacings of 3.14Å and 1.92Å), but not the 311 beams (at 1.64Å).

cutoff frequency (eqn 18), but represents information in the amplitude spectrum out to only the convergence cutoff frequency.

It is clear that HRTEM resolution will continue to improve. In the case of structure-image resolution (Scherzer resolution), advances will proceed by a combination of instrumental improvement and increased reliance on processing of focus series of images captured precisely with CCD cameras and immediately digitized. Hopefully, such processing will approach "real-time" as microscopes incorporate more computer control, image processing algorithms improve, and computer hardware becomes more powerful. Because the ultimate limit on information transfer is imposed by the microscope spread of focus (eqn 17), improvements in C_C, power supply stability, and energy spread will play a large part in future advances for conventional HRTEMs. Other approaches to improved image coherence, such as FEGs and energy-filtered imaging, promise to play a significant role.

Acknowledgements

Thanks are due to J.C.H. Spence for his input to the seminal abstract [1], and to M. Sarikaya and R.M. Fisher for critical reading of the manuscript. This work was supported by the Director, Office of Energy Research, Office of Basic Energy Sciences, Materials Science Division, U.S. Department of Energy under Contract No. DE AC-03-76SF00098.

Table 1. HRTEMs with point-to-point resolution better than 2.5Å[a]

Microscope	Maximum operating energy (keV)	C_s (mm)	C_c (mm)	Scherzer resolution (Å)	
				Theoretical[b]	Demonstrated[c]
Cambridge HREM	600	2.5	2.7	1.70	1.8
Hitachi H800	200	1.0	1.2	2.26	2.3
Hitachi HF2000[f]	200	1.2	1.4	2.37	
Hitachi H9000-UHR	300	0.9	1.5	1.84	1.9
Hitachi H9000-NAR	300	0.7	1.4	1.73	1.8
Hitachi HU1250	1250	2.5	3.5	1.13	1.5
Hitachi H-1500	1300	1.85	3.4	1.03	1.4
ISI[d] 002A	120	0.3	0.6	2.08	2.2
ISI[d] 002B	200	0.4	0.8	1.80	2.0
JEOL 2000EX	200	0.9	1.2	2.21	2.3
JEOL 2010HT	200	1.0	1.4	2.26	2.3
JEOL 2010UHR	200	0.5	1.0	1.90	2.0
JEOL 2010F[f]	200	0.5	1.0	1.90	2.0
JEOL 3010HT	300	1.4	2.2	2.05	
JEOL 3010UHR	300	0.6	1.4	1.66	1.7
JEOL 4000EX	400	0.9	1.65	1.61	1.7
JEOL HAREM	500	1.0	1.4	1.48	1.8
JEOL ARM-1000	1000	2.3	3.4	1.26	1.6
JEOL Kyoto-1000	1000	1.7	3.6	1.17	1.5
JEOL ARM-1250	1250	1.6	4.0	1.02	1.4
Philips CM20/ST[e]	200	1.2	1.2	2.37	2.4
Philips CM20/UT[e]	200	0.5	1.0	1.90	2.0
Philips CM30/T	300	2.0	2.3	2.25	2.3
Philips CM30/ST	300	1.2	1.5	1.98	2.0

[a]Adapted from Table 12.1 of reference [31]

[b]CTF crossover at a defocus of 1.225 Scherzers

[c]Where known -- approximate figure only

[d]Now TopCon

[e]May be equipped with field emission gun (FEG)

[f]Equipped with field emission gun (FEG)

References

[1] Michael A. O'Keefe and John C.H. Spence, Proc. 49th Ann. Meeting EMSA, San Jose, California (1991) 498-599.

[2] J. Fertig and H. Rose, Optik **54** (1979) 165-191.

[3] J.M. Cowley, Chemica Scripta **14** (1978) 33-38.

[4] S.J. Pennycook and L.A. Boatner, Nature **336** (1985) 565.

[5] M.A. O'Keefe, Acta Cryst. A**29** (1973) 389-401.

[6] A.R. Smith and L. Eyring, Ultramicroscopy **8** (1982) 65-78

[7] J.C.H. Spence, Experimental high-resolution electron microscopy. 2nd ed. (Oxford University Press, New York, 1988).

[8] M.A. O'Keefe, Proc. 37th Ann. Meeting EMSA, San Antonio, Texas (1979) 556-557.

[9] M.A. O'Keefe and W.O. Saxton, Proc. 41st Ann. Meeting EMSA, Phoenix, Arizona (1983) 288-289.

[10] J. Frank, Optik **38** (1973) 519-536.

[11] R.H. Wade and J. Frank, Optik **49** (1977) 81-92.

[12] F.A. Ponce and M.A. O'Keefe, Proc. 44th Ann. Meeting EMSA, Albuquerque (1986) 522-525.

[13] O. Scherzer, J. Appl. Phys. **20** (1949) 20.

[14] M.A. O'Keefe, Proc. 3rd Pfefferkorn Conf. on Electron Optical Systems, Ocean City, Maryland (Scanning Microscopy International, Chicago, 1984) 209-220.

[15] M.A. O'Keefe, P.R. Buseck and S. Iijima, Nature **274** (1978) 322-324.

[16] J.M. Cowley, and S. Iijima, Z. Naturforsch. 27a (1972) 445-451.

[17] J.M. Cowley, Diffraction Physics (North-Holland/American Elsevier, New York, 1975)

[18] M.A. O'Keefe and A. J. Pitt, Electron Microscopy 1980. (Proc. 7th European Cong. on Electron Microscopy, The Hague, Netherlands, 1980) 122-123 .

[19] C.B. Eisenhandler and B.J. Siegel, J. Appl. Phys. **37** (1966) 1613-1620.

[20] M.A. O'Keefe and J.V. Sanders, Acta Cryst. A**31** (1975) 307-310.

[21] R.M. Fisher and T. Imura, Ultramicroscopy **3** (1978) 3-18.

[22] P. Fejes, Acta Cryst. A**33** (1977) 109-113.

[23] K. Ishizuka, Ultramicroscopy **5** (1980) 55-65.

[24] D.J. Smith and M.A. O'Keefe, Acta Cryst. A**39** (1983) 139-148.

[25] G.R. Anstis and M.A. O'Keefe, Proc. 34th Ann. Meeting EMSA, Miami Beach, Florida (1976) 480-481.

[26] E.J. Kirkland, Ultramicroscopy **15** (1984) 151-172.

[27] D. Van Dyck and M. Op de Beeck, Proc. XIIth Int. Congress for Electron Microscopy, **1** (1990) 26-27.

[28] W. Dong, T. Baird, J.R. Fryer, C.J. Gilmore, D.D. MacNicol, G. Bricogne, D.J. Smith, M.A. O'Keefe and S. Hovmöller, Nature **355** (1992) 605-609.

[29] Kenneth H. Downing, Hu Meisheng, Hans-Rudolf Wenk and Michael A. O'Keefe, Nature **348** (1990) 525-528.

[30] H-R. Wenk, K.H. Downing, Hu Meisheng, and M.A. O'Keefe, (1992) Acta Cryst. accepted.

[31] O.L. Krivanek, in: High-Resolution Transmission Electron Microscopy and Associated Techniques, Eds. Peter Buseck, John Cowley and LeRoy Eyring (OUP, New York, 1992) p.521.

Figure Captions

Fig. 1. Illustration of the formation of the image intensity spectrum from five co-linear beams out to $|\mathbf{k}|=\pm 2$. (a) In the general case (eqn 2), an image amplitude spectrum with five components generates an image intensity spectrum $I(\mathbf{k})$ with nine components, out to $|\mathbf{k}| =\pm 4$. Interferences contributing to each to each of the nine components are tabulated in abbreviated form, with n.m representing the contribution from $\Psi(\mathbf{n}).\Psi^*(\mathbf{m})$. (b) Under the WPO approximation (eqn 4), the non-linear interferences are neglected, and $I_L(\mathbf{k})$ contains only five components, out to $|\mathbf{k}| =\pm 2$. No "half-plane" terms are generated, and each linear-image intensity component is the sum of only two interferences. Note the many missing interference terms compared with the general case (a). XBL 925-1071

Fig. 2. Argand diagrams showing the action of $\sin\chi(\mathbf{k})$ under WPO conditions. (a) Formation of the kth image amplitude component $\Psi(\mathbf{k})$. The specimen potential component $V(\mathbf{k})$ gives rise to an exit-surface diffracted beam $\Psi_E(\mathbf{k})$ at a phase difference of $-\pi/2$ from $V(\mathbf{k})$. Passage through the objective lens rotates the phase of $\Psi_E(\mathbf{k})$ through an angle of $\chi(\mathbf{k})$ to form $\Psi(\mathbf{k})$. (b) Formation of the second amplitude component contributing to the kth image intensity component. (c) Summation of the two amplitude components to produce the intensity component $I_L(\mathbf{k})$, which lies along the negative extension of the original $V(\mathbf{k})$ and has an amplitude (length) proportional to $2\sin\chi(\mathbf{k})$. XBL 925-1072

Fig. 3. Phase-contrast transfer functions (CTFs), plotted out to a frequency corresponding to 1.4Å, at defocus values of one Scherzer and $\sqrt{1.5}$ Scherzers. At one Scherzer (a), the passband is flat with a transfer value of -1 at the minimum; for 400keV and a 0.9mm C_S, crossover is at 1.78Å. At $\sqrt{1.5}$ Scherzers (b), the passband has a transfer of better than 70% over the marked passband region, and extends out to a resolution of 1.68Å. XBL 925-1073

Fig. 4. CTFs (solid lines) out to 1.4Å at an "optimum" defocus values of $\sqrt{1.5}$ Scherzers, showing the effects of multiplication by the damping envelopes (dashed lines). (a) The convergence envelope $E_\alpha(\mathbf{k})$ for a value of the semi-angle of convergence α of 1milliradian. (b) The envelope $E_\Delta(\mathbf{k})$ for a spread-of-focus halfwidth Δ of 60Å. (c) The combined effect of the two envelope functions. XBL 925-1074

Fig. 5 Structure images of $Nb_{12}O_{29}$ taken at (a) 100keV (S. Iijima) and (b) 1000keV (S. Horiuchi) under WPO conditions. Matching SHRLI simulations are inset at lower left in each image. Damping envelopes or aperture functions (AF) are shown for both HRTEMs, with objective aperture (A), spread-of-focus envelope (B), convergence envelope (C), and overall damping function (D). Spatial frequency (k) is marked in reciprocal Ångstrom units. (Published as fig.1 in ref [21]) XBB 848-6142

Fig. 6. CTFs (solid lines) out to 1.2Å for a convergence of 1 milliradian. (a) At a defocus value of √1.5 Scherzers with Δ=0. (b) At a defocus value of √5.5 Scherzers with Δ=0. (c) At defocus values of √1.5, √3.5, √5.5, √7.5 and √9.5 Scherzers with Δ=60Å; the damping envelope (dashed lines) is plotted for a spread-of-focus halfwidth Δ of 60Å and zero convergence, and envelopes all the attainable CTFs. XBL 925-1075

Fig. 7. Transmission cross coefficient damping functions [8], for convergence (upper) and spread-of-focus (lower); white means high transference. In each case, (a) is the generalized function, (b) is the linear-image function, and (c) is the difference. The amount of damping for any interference $\Psi(\mathbf{n}).\Psi^*(\mathbf{m})$ is found by moving $|\mathbf{n}|$ up and $|\mathbf{m}|$ across from the origin (center) of each plot. For linear-image interferences, one of $|\mathbf{n}|$ and $|\mathbf{m}|$ is zero, and the damping is read along a horizontal (or vertical) line giving a profile of the linear-image damping function (see insert in the linear-image convergence plot). The positions of the three interferences making up the $\overline{2}$ component of the image intensity spectrum of figure 1a are plotted on the spread-of-focus damping function. XBB 848-6145

Fig. 8. Phase contrast transfer functions (CTFs) for a mid-voltage HRTEM (curve 1), and two high-voltage HRTEMs (curves 2 & 3). Operating conditions are listed above the plots; the spatial frequency scale and CTF cross-overs are given in Ångstrom units. XBL 925-1076

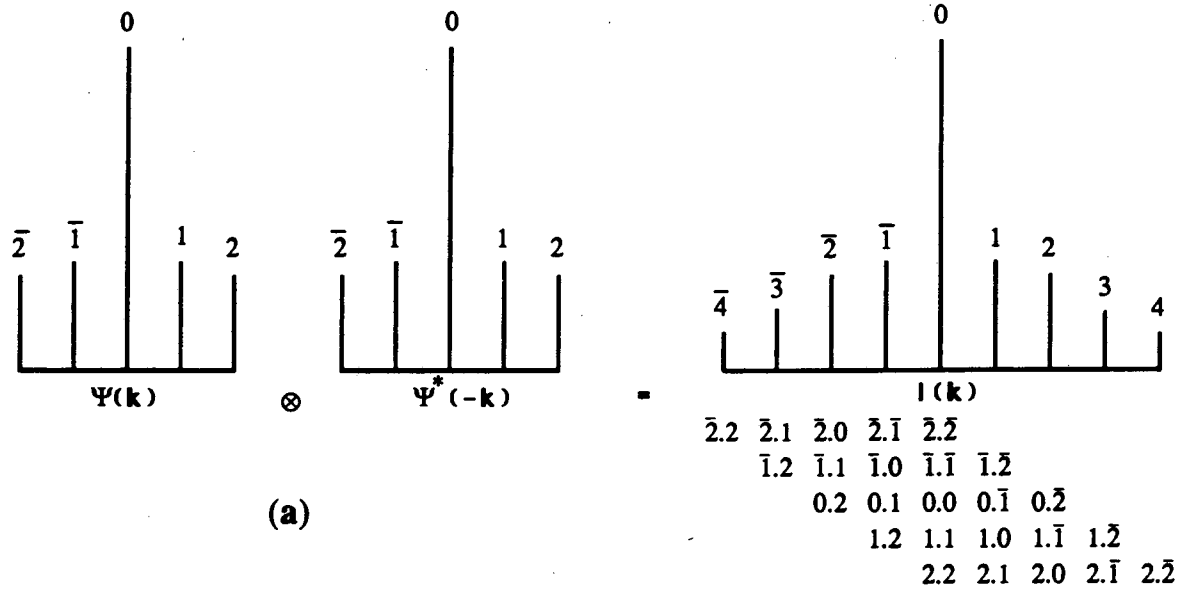

(a)

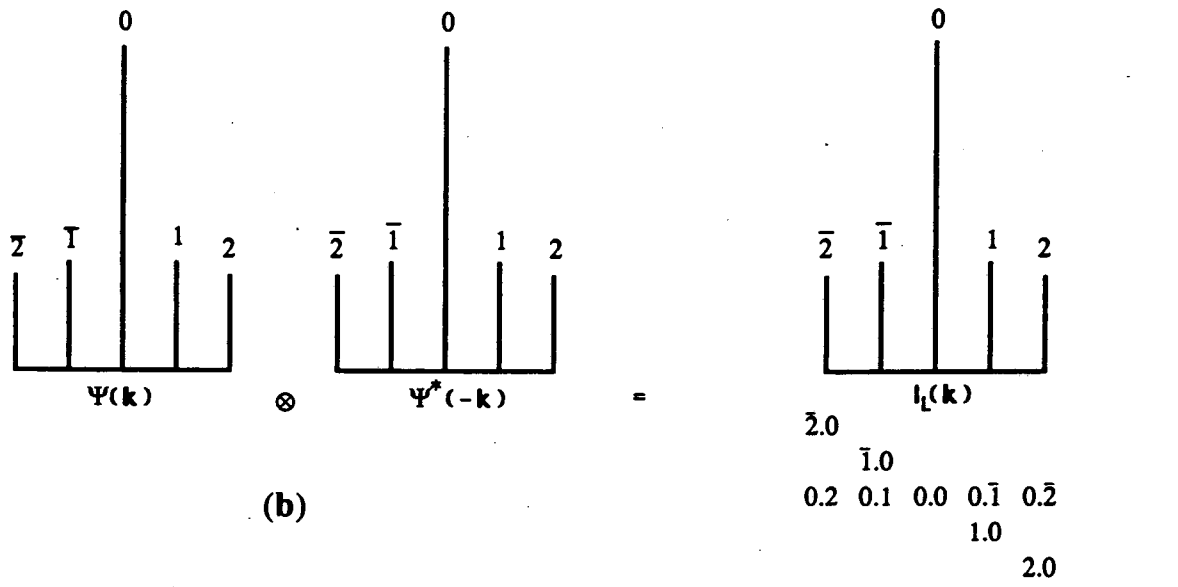

(b)

XBL 925-1071

Figure 1

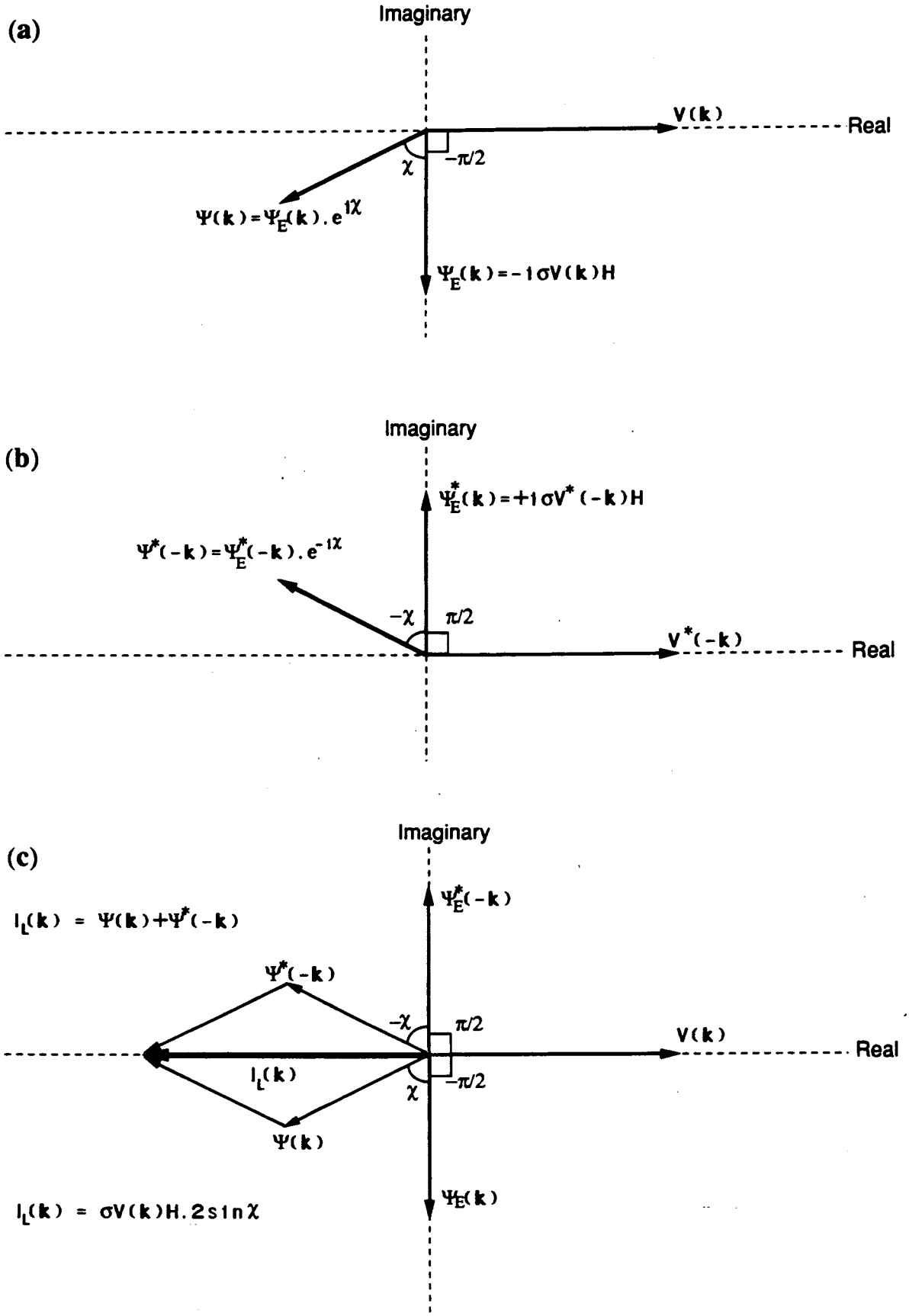

Figure 2

XBL 925-1072

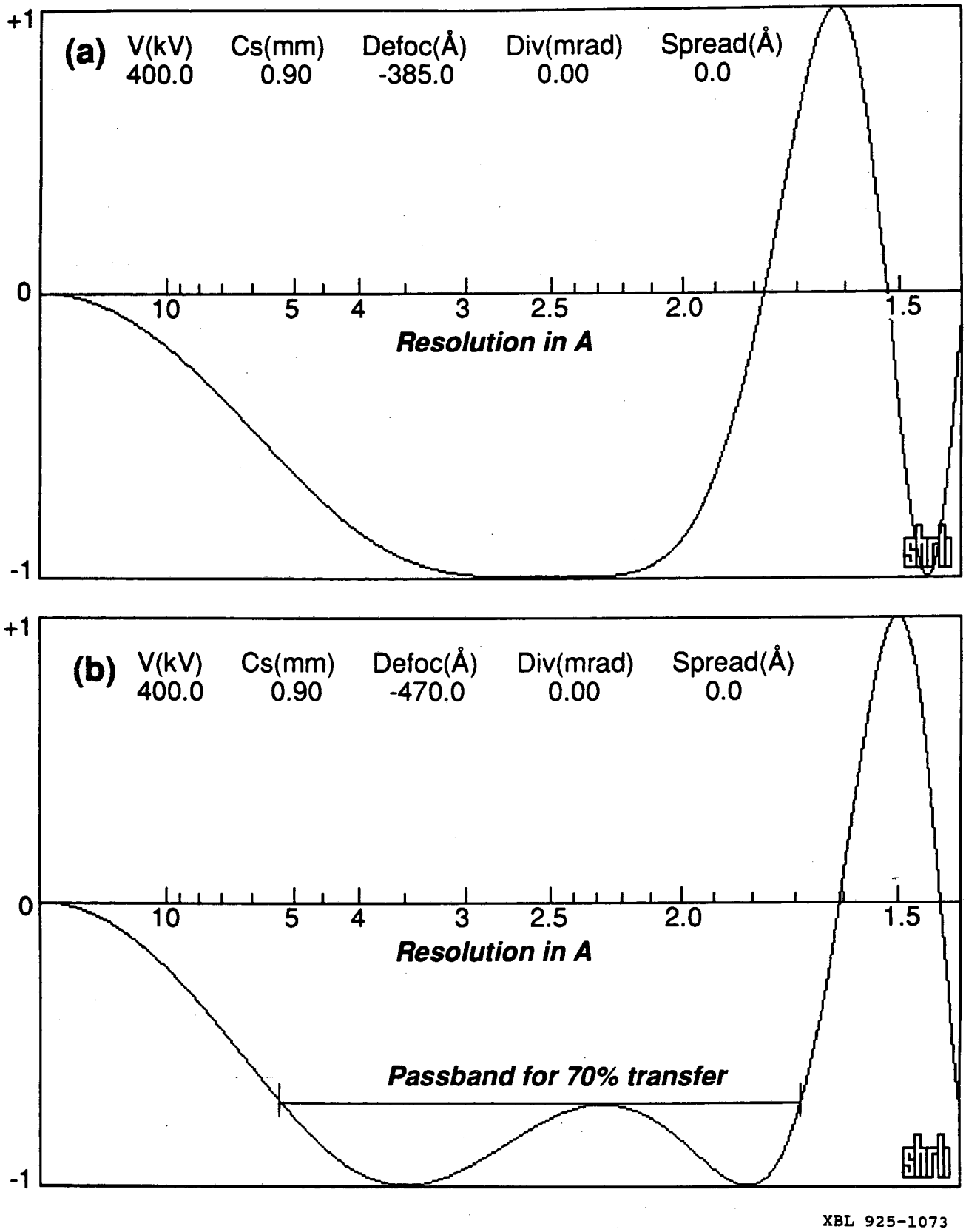
(a)
V(kV) 400.0
Cs(mm) 0.90
Defoc(Å) -385.0
Div(mrad) 0.00
Spread(Å) 0.0
+1
0
-1
10
5
4
3
2.5
2.0
1.5
Resolution in A
(b)
V(kV) 400.0
Cs(mm) 0.90
Defoc(Å) -470.0
Div(mrad) 0.00
Spread(Å) 0.0
Passband for 70% transfer
XBL 925-1073

Figure 3

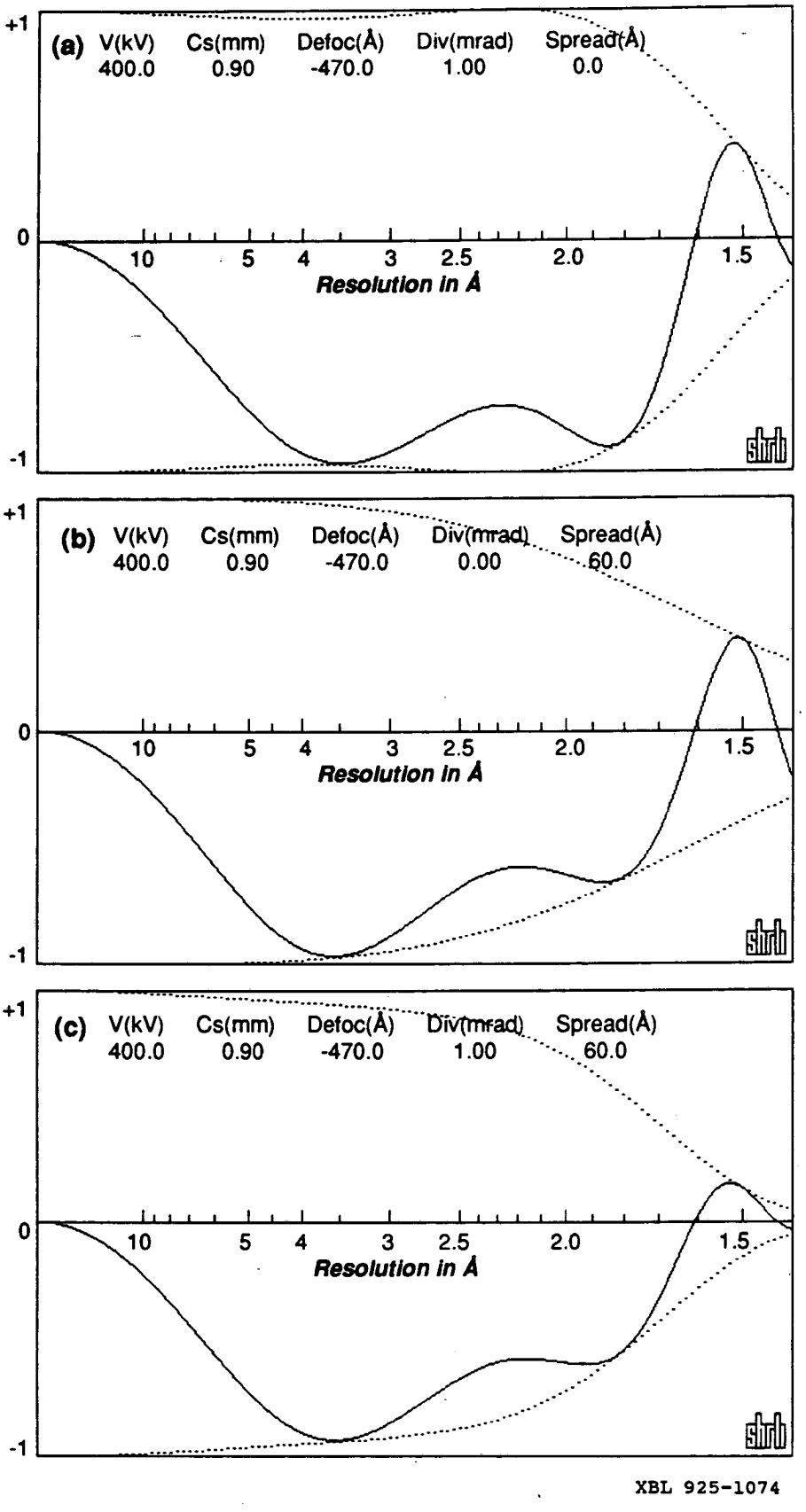
(a) V(kV) Cs(mm) Defoc(Å) Div(mrad) Spread(Å)
400.0 0.90 -470.0 1.00 0.0
+1
0
-1
10 5 4 3 2.5 2.0 1.5
Resolution in Å
(b) V(kV) Cs(mm) Defoc(Å) Div(mrad) Spread(Å)
400.0 0.90 -470.0 0.00 60.0
+1
0
-1
10 5 4 3 2.5 2.0 1.5
Resolution in Å
(c) V(kV) Cs(mm) Defoc(Å) Div(mrad) Spread(Å)
400.0 0.90 -470.0 1.00 60.0
+1
0
-1
10 5 4 3 2.5 2.0 1.5
Resolution in Å
XBL 925-1074

Figure 4

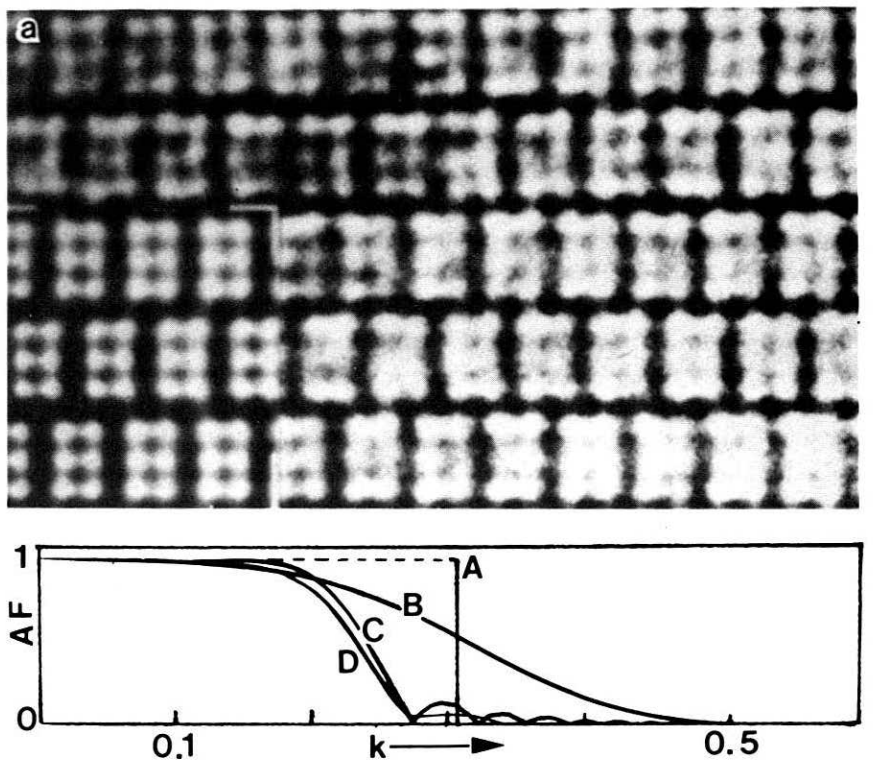

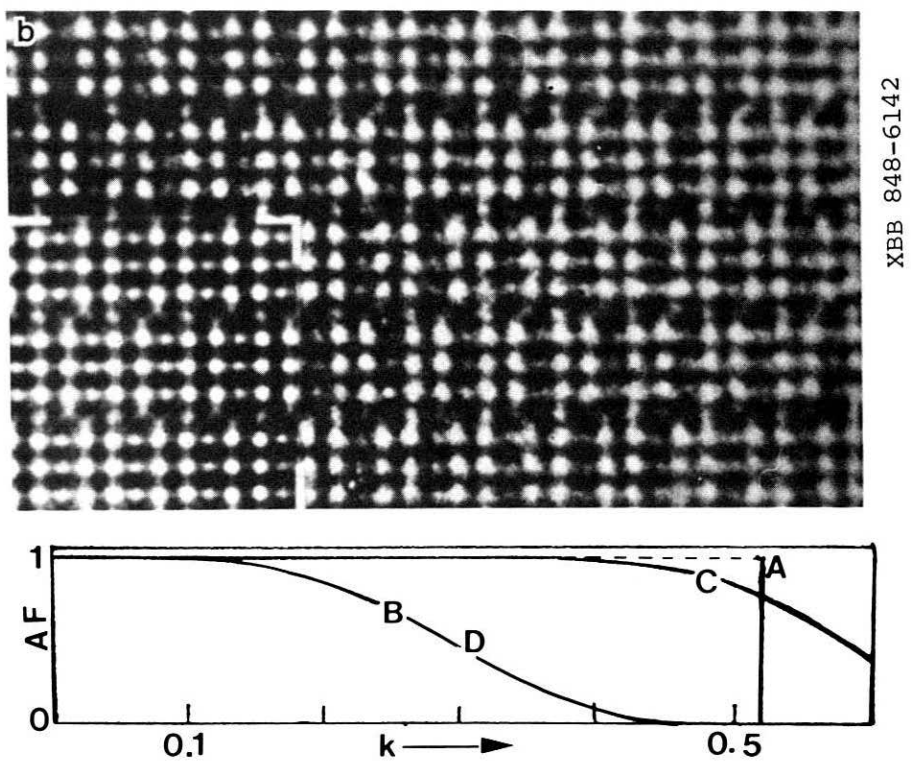

XBB 848-6142

Figure 5

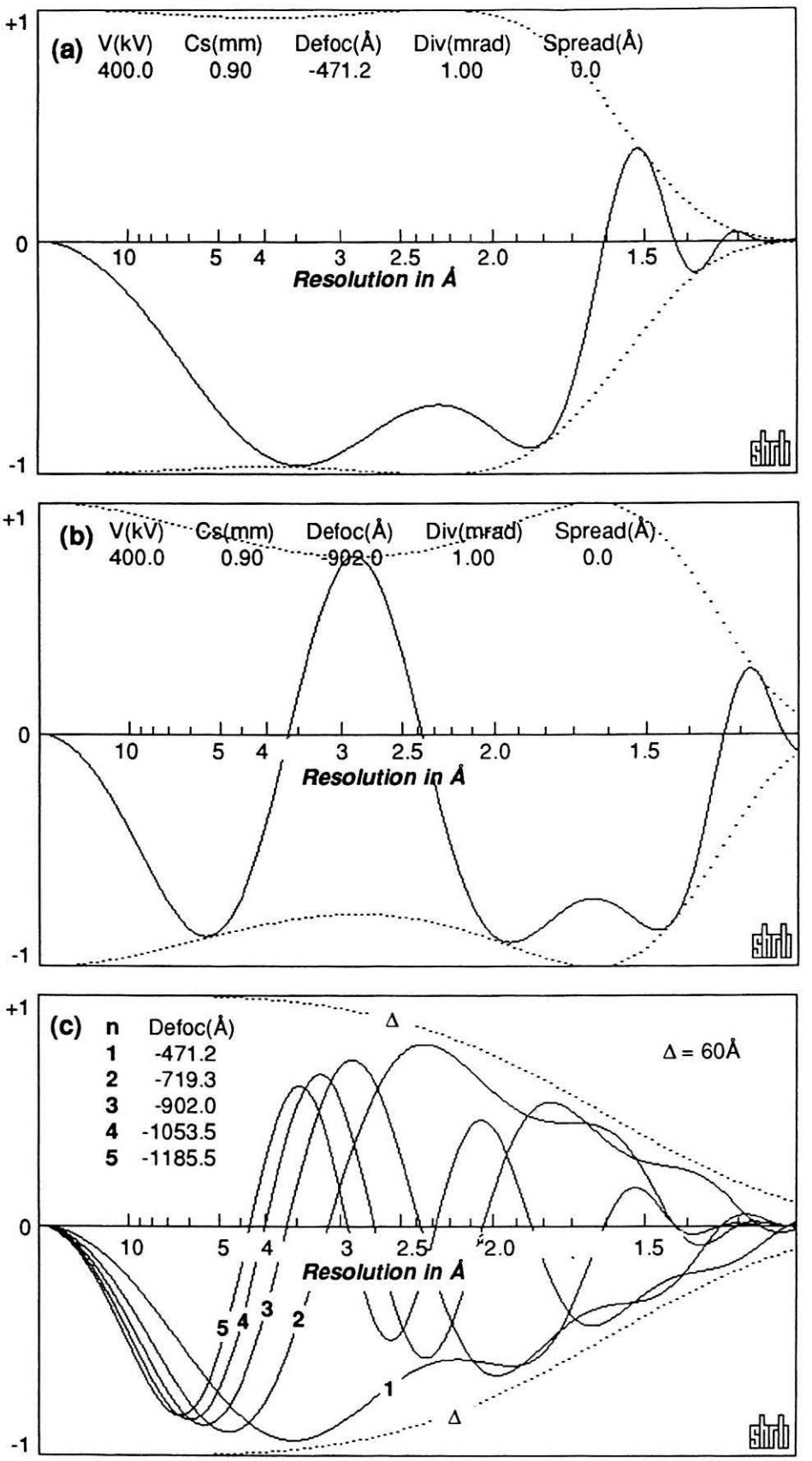

XBL 925-1075

Figure 6

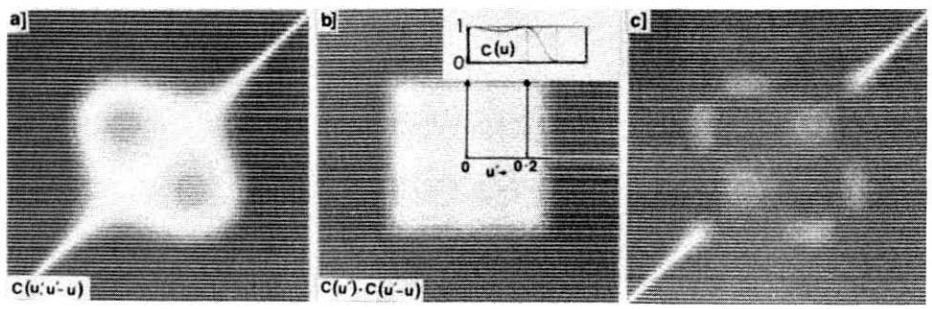

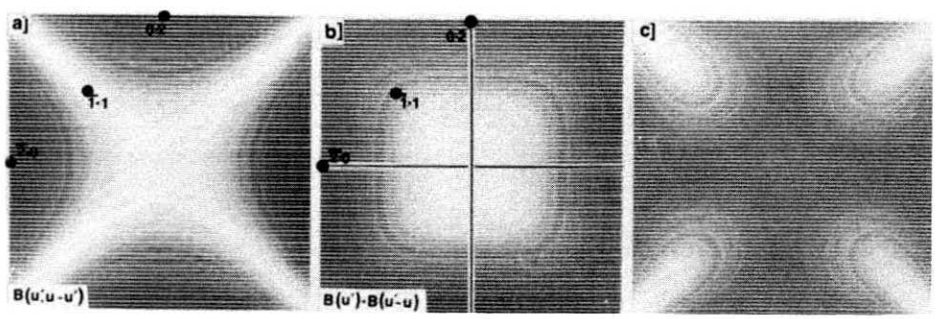

XBB 847-6145

Figure 7

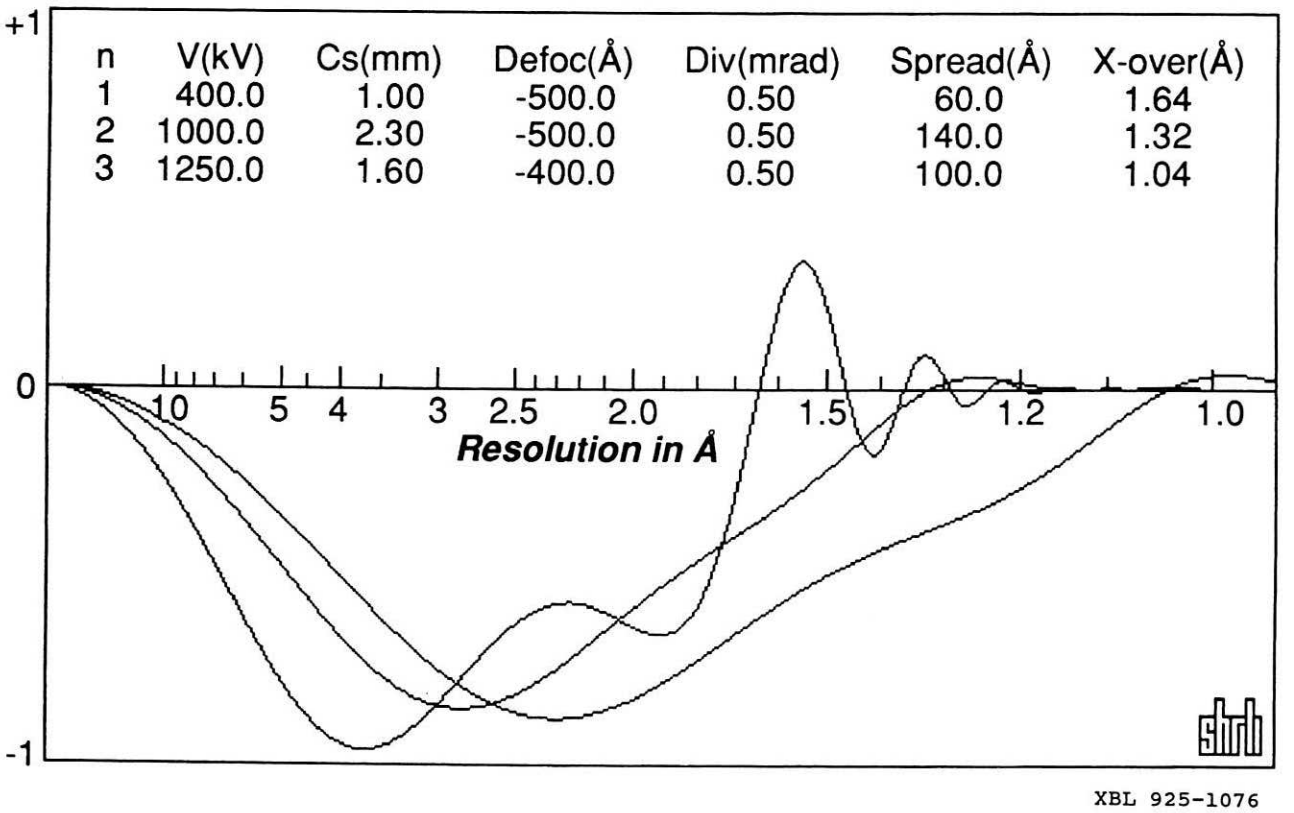
+1
0
-1
n V(kV) Cs(mm) Defoc(Å) Div(mrad) Spread(Å) X-over(Å)
1 400.0 1.00 -500.0 0.50 60.0 1.64
2 1000.0 2.30 -500.0 0.50 140.0 1.32
3 1250.0 1.60 -400.0 0.50 100.0 1.04
10 5 4 3 2.5 2.0 1.5 1.2 1.0
Resolution in Å
XBL 925-1076

Figure 8

LAWRENCE BERKELEY LABORATORY
UNIVERSITY OF CALIFORNIA
TECHNICAL INFORMATION DEPARTMENT
BERKELEY, CALIFORNIA 94720